nature materials

LETTERS

PUBLISHED ONLINE: 12 JUNE 2017 | DOI: 10.1038/NMAT4915

Intrinsically patterned two-dimensional materials for selective adsorption of molecules and nanoclusters

X. Lin[1†], J. C. Lu[1†], Y. Shao[1†], Y. Y. Zhang[1,2†], X. Wu[1], J. B. Pan[1], L. Gao[1], S. Y. Zhu[1], K. Qian[1], Y. F. Zhang[1], D. L. Bao[1], L. F. Li[1], Y. Q. Wang[1], Z. L. Liu[1], J. T. Sun[1], T. Lei[3], C. Liu[3], J. O. Wang[3], K. Ibrahim[3], D. N. Leonard[4], W. Zhou[1,4], H. M. Guo[1], Y. L. Wang[1]*, S. X. Du[1]*, S. T. Pantelides[1,2] and H.-J. Gao[1]*

Two-dimensional (2D) materials have been studied extensively as monolayers[1–5], vertical or lateral heterostructures[6–8]. To achieve functionalization, monolayers are often patterned using soft lithography and selectively decorated with molecules[9,10]. Here we demonstrate the growth of a family of 2D materials that are intrinsically patterned. We demonstrate that a monolayer of $PtSe_2$ can be grown on a Pt substrate in the form of a triangular pattern of alternating 1T and 1H phases. Moreover, we show that, in a monolayer of CuSe grown on a Cu substrate, strain relaxation leads to periodic patterns of triangular nanopores with uniform size. Adsorption of different species at preferred pattern sites is also achieved, demonstrating that these materials can serve as templates for selective self-assembly of molecules or nanoclusters, as well as for the functionalization of the same substrate with two different species.

Two-dimensional (2D) materials have unique and unusual properties that promise novel applications[6,11,12]. Typically, 2D materials need to be functionalized and patterned, just as semiconductor films need to be doped n-type or p-type in a lithographically patterned way to produce p–n junctions (light-emitting diodes, junction lasers, resistors) and transistor structures[10,11]. Functionalization of 2D materials is done in a variety of ways, for example, by doping with impurities or molecules, either within the 2D lattices or adsorbed on the exposed surfaces[10]. In particular, functionalization by adsorbates can facilitate catalysis, sensing, optical or magnetic response, nanodevices, or other applications. To achieve selective or multiple functionalization by adsorbates, patterning by soft lithography has been used[9]. 2D materials exhibiting forms of atomic-scale patterning have been proposed on the basis of calculations by the choice of Bravais lattice[13] or stoichiometry[14,15]. Moiré patterns represent a nanoscale form of patterning imposed by the substrate on otherwise homogeneous 2D materials[16,17].

Herein, we report the fabrication of prototypes of a family of 2D materials that are intrinsically patterned on the nanoscale and can be selectively or dually functionalized by adsorbates. We report two prototype 2D materials, each obtained by direct selenization of a monatomic metal substrate. More specifically, we show that, by controlling the annealing temperature and deposition amount of Se on a Pt substrate, we obtain either a homogeneous monolayer $PtSe_2$ in the 1T phase or a 'patterned monolayer' comprising a periodic triangular structure of alternating 1H and 1T phases. The size of the triangles can be tuned by varying the density of deposited Se atoms. The choice between a homogeneous 1T phase or patterned 1H/1T phases is reversible. We also report the fabrication of a patterned monolayer of CuSe having periodic arrays of triangular nanopores, with distinct domains. In both patterned materials, adsorption of different species at preferred pattern components has been achieved, illustrating the potential for selective/dual functionalization. In the above two prototype intrinsically patterned monolayers, we show that $Fe_{13}Se_7$ nanoclusters, a known catalyst[18], can be grown selectively in the nanopores of patterned CuSe monolayer, providing a way to avoid aggregation in nanoparticle catalysts. Another molecular species, iron(II) phthalocyanine (FePc), can be selectively adsorbed on the CuSe surface between the nanopores. Throughout the exposition we use density functional theory (DFT) calculations to account for the observations.

A prototype of a 2D intrinsically patterned material is shown schematically in Fig. 1a. The entire monolayer is $PtSe_2$, but the two distinct types of triangle are two different phases, 1H and 1T (blue and yellow triangles, respectively). A large-scale scanning tunnelling microscope (STM) image of such a structure is shown in Fig. 1b. We will describe shortly how the patterned structure was fabricated and how we determined that the two kinds of moiré pattern, exhibiting honeycomb and hexagonal features, are the 1H and 1T phase of $PtSe_2$, respectively. The honeycomb and hexagonal structures are more visible in the intermediate-resolution STM images of Fig. 1c–e. These images also demonstrate that triangles of different sizes are possible. Atomic-resolution images are shown in Fig. 1f–h, together with simulations in Fig. 1i–k. The detailed structures are shown in Supplementary Figs 1–3. A clean, sharp interface is clearly visible in Fig. 1g.

The formation of a homogeneous monolayer 1T $PtSe_2$ on a Pt(111) substrate by direct selenization has been described in ref. 19. Such a monolayer, fabricated by annealing at 270 °C during the selenization of a Pt substrate, is shown in Fig. 2a. A homogeneous 1T sample transforms to a triangular pattern (Fig. 2c) by annealing at 400 °C. This elevated temperature leads to the loss of some selenium, leaving vacancies (marked by the yellow arrow) in the film. The transformation process is monitored by the change of chemical states of Se atoms via *in situ* X-ray photoelectron spectroscopy (XPS) measurements. As shown in Fig. 2b, the Se 3*d* core level from the pure 1T structure $PtSe_2$ monolayer exhibits two peaks (coloured in red). After annealing the sample to 400 °C, the intensity of the initial

[1]Institute of Physics & University of Chinese Academy of Sciences, Chinese Academy of Sciences, Beijing 100190, China. [2]Department of Physics and Astronomy and Department of Electrical Engineering and Computer Science, Vanderbilt University, Nashville, Tennessee 37235, USA. [3]Institute of High Energy Physics, Chinese Academy of Sciences, Beijing 100049, China. [4]Material Sciences and Technology Division, Oak Ridge National Laboratory, Oak Ridge, Tennessee 37381, USA. †These authors contributed equally to this work. *e-mail: ylwang@iphy.ac.cn; sxdu@iphy.ac.cn; hjgao@iphy.ac.cn

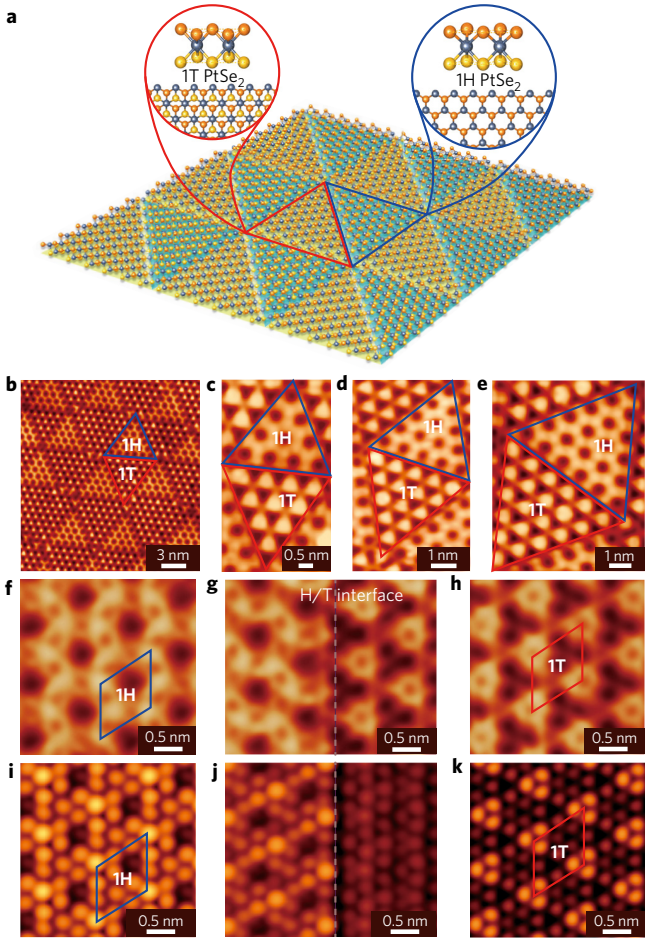

Figure 1 | 1H/1T tiling pattern in monolayer $PtSe_2$. a, Schematic illustration of the triangular tiling pattern formed by alternating 1H and 1T $PtSe_2$ areas, which are coloured blue and yellow, respectively. Two views of atomic models for the two configurations are shown in the respective insets. The top-layer Se atoms, Pt atoms and the bottom-layer Se atoms are coloured orange, blue and yellow, respectively. **b**, STM image of the 1H/1T patterned structure in monolayer $PtSe_2$. $V_s = -1.6$ V, $I_t = 0.1$ nA. **c**–**e**, STM images of 1H and 1T $PtSe_2$ domains of different sizes. $V_s = -1.6$ V, $I_t = 0.5$ nA. **f**–**h**, High-resolution STM images of 1H $PtSe_2$ (**f**), 1H/1T interface (**g**) and 1T $PtSe_2$ (**h**). The unit cells of the 1H and 1T domains are marked by blue and red diamonds, respectively. $V_s = -1.0$ V, $I_t = 0.8$ nA. **i**–**k**, STM simulations of a 1H $PtSe_2$ domain (**i**), the 1H/1T interface (**j**) and a 1T $PtSe_2$ domain (**k**).

red peaks decreases and two new peaks (coloured in blue) appear. The new peaks have an energy shift of 0.4 eV relative to the initial ones. Considering that a similar energy shift in the XPS spectra has been reported between H and T phases in $MoTe_2$ flakes[11], the XPS energy shift (Fig. 2b) in $PtSe_2$ is consistent with a local 1T-to-1H transformation. Theoretical calculations indicate that free-standing 1H $PtSe_2$ monolayer is not stable (Supplementary Fig. 4). For the patterned structure with alternating triangular 1T and 1H areas, the 1H domains are limited in size and are probably stabilized by the surrounding 1T $PtSe_2$.

We also measured $I(z)$ spectra, which provide information on the local workfunction. As shown in Supplementary Fig. 5, the derived workfunction in 1T domains is larger than that in 1H domains, which is confirmed by DFT calculations. These results provide further evidence of the existence of 1H $PtSe_2$.

The transformation of a pure 1T phase to a patterned 1H/1T phase is reversible. By adding Se atoms and annealing the sample to ~270 °C, the triangular pattern reverts to a defect-free homogeneous 1T structure (Fig. 2a). The extra peaks in the XPS spectrum of the patterned 1H/1T phase (blue peaks in Fig. 2b) also disappear, confirming that the sample reverts to a pure 1T structure. The disappearance of the Se vacancies during the reversible transformation provides evidence that Se vacancies mediate the formation of 1H domains.

On the basis of the above experimental data, we use the schematic drawings in Fig. 2d–g, to show the transformation process and mechanism. Specifically, thermal annealing of a pristine 1T structure $PtSe_2$ film at an elevated temperature leads to the loss of top-layer Se atoms (depicted by the arrow in Fig. 2c), generating Se vacancies (Fig. 2e). DFT calculations find that lines of vacancies are energetically preferred (see Supplementary Fig. 6), which is in agreement with a previous report[20]. Because of the threefold point symmetry, three directions of such lines are possible, which leads to the formation of triangles, as shown in Fig. 2f. Within the triangle surrounded by vacancies, a transformation of the 1T phase to the 1H phase occurs and leads to a 1H/1T patterned structure. A similar structural transformation has been reported in a MoS_2 monolayer[21]. More details of the 1T-to-1H transformation in $PtSe_2$ can be found in Supplementary Figs 6 and 7.

An alternative method to produce the 1H/1T triangular pattern is to control the initial density of Se atoms. This process is shown schematically in Supplementary Fig. 8. For the fabrication of a homogeneous 1T $PtSe_2$, the crucible is filled with the Se source and held at-centre for a long time to deliver ample amounts of Se everywhere on the sample. The 1H/1T triangular pattern is fabricated by holding the crucible filled with the Se source off-centred to the substrate, resulting in a Se density gradient, which subsequently leads to different structures. A triangular tiling pattern of 1H/1T $PtSe_2$ forms in the area with a relatively low Se density. As the density of Se atoms increases, the size of 1T $PtSe_2$ triangles increases and the number of 1H $PtSe_2$ triangles decreases significantly. As the Se density increases further, it eventually leads to a defect-free homogeneous 1T $PtSe_2$ film. An intermediate structure can be found in between the 1H/1T tiling region and the homogeneous 1T region. Typical STM images with different Se amounts are shown in Supplementary Fig. 8. The XPS mapping of Se 3*d* electrons along the direction of increasing Se density areas (area circled one to area circled four) confirms a significant decrease of 1H $PtSe_2$ and increase of 1T $PtSe_2$. These data confirm the role of Se vacancies and suggest that a critical concentration is necessary to produce a periodic triangular pattern.

The highly ordered triangular tiling patterns constructed by 1H and 1T phases of a monolayer $PtSe_2$ make it a suitable template for selective adsorption of different species. Figure 2h,i shows a large-scale area and zoomed-in images of pentacene ($C_{22}H_{14}$) on patterned $PtSe_2$. It is clear that pentacene molecules adsorb selectively on 1H triangles, allowing the formation of a periodic array of molecules. The high-resolution STM image shown in Fig. 2i demonstrates more details for the nanoclusters, which present three orientations corresponding to the triangular shape of the 1H $PtSe_2$ region.

The preference of molecules to bind on the 1T or 1H domain is determined by the relative binding energies. As shown in Supplementary Table 1, all of the tested molecules have larger binding energies on the 1H domain. The basic idea, nevertheless, is that different molecules can in principle adsorb on the two phases of an intrinsically patterned 2D material, leading to simultaneous dual functionalization for catalysis or other applications. The possibility of different objects adsorbing on different regions of a patterned material will be demonstrated in the next prototype intrinsically patterned 2D material, namely monolayer CuSe on a Cu substrate.

In addition to 1H/1T patterned $PtSe_2$, we have fabricated an intrinsically patterned form of monolayer CuSe by direct selenization of Cu(111) substrate (more details of the fabrication process are given in Supplementary Information). A large-scale STM image of a monolayer CuSe with periodic arrays of identical

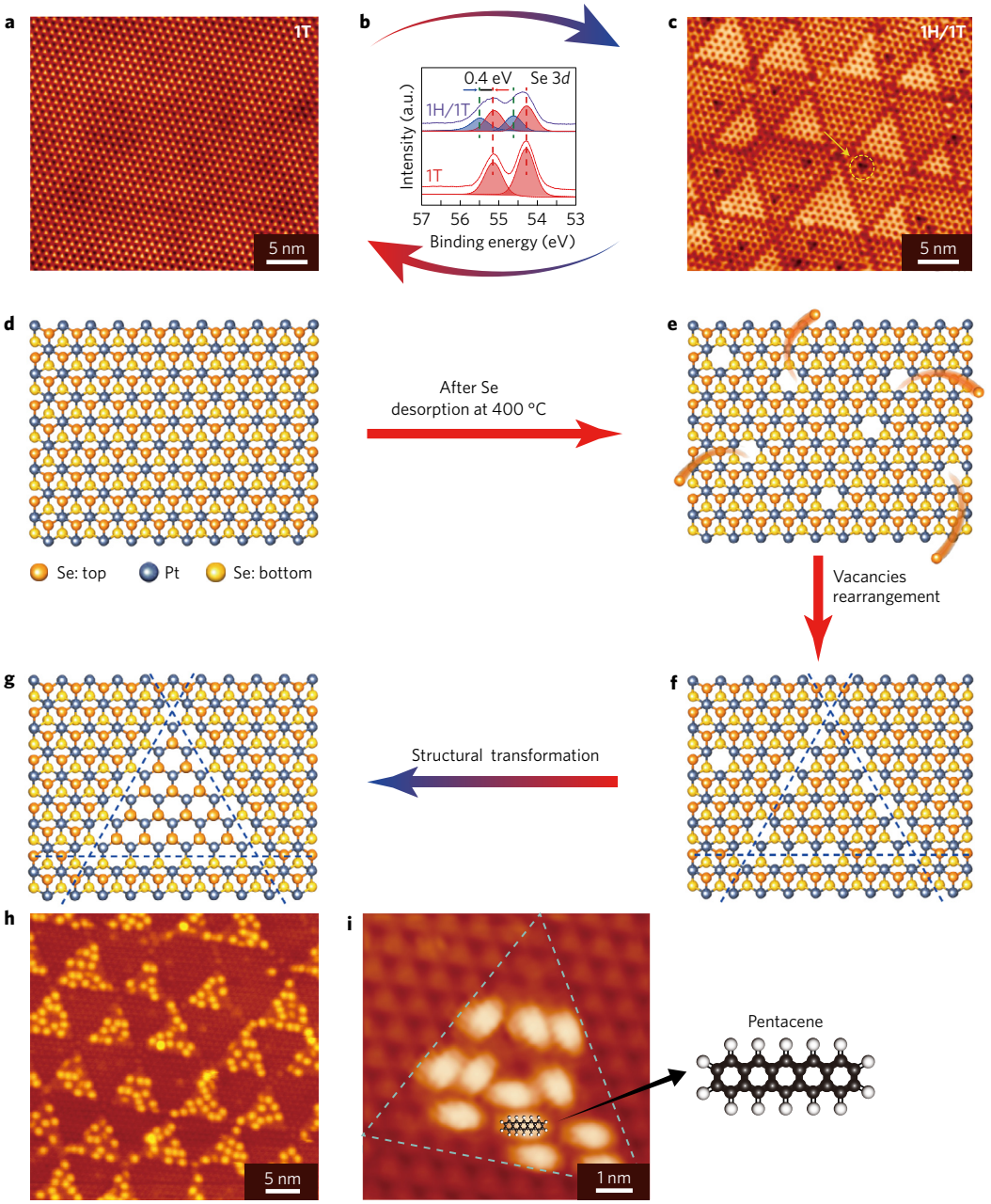

Figure 2 | Reversible transition and selective adsorption of 1H/1T tiling pattern. a,**c**, Typical STM images of pure 1T $PtSe_2$ (**a**) and 1H/1T patterned $PtSe_2$ (**c**). The 1H/1T tiling structure can be obtained from a pure 1T structure by annealing the sample to 400 °C. The reverse process (from 1H/1T tiling to pure 1T structure) can be realized by adding Se and annealing at 270 °C. $V_s = -1.6$ V, $I_t = 0.1$ nA. **b**, The XPS spectra of Se 3*d* electrons for the entire reversible structural transformation process. The red and purple peaks originate from Se 3*d* electrons in 1T and 1H $PtSe_2$ films with a 0.4 eV shift, respectively. **d**–**g**, Schematic illustration of the structural transformation from pure 1T $PtSe_2$ to 1H/1T patterned $PtSe_2$. The formation of 1H $PtSe_2$ domains is a result of the collective evolution of Se vacancies. **h**, An STM image of pentacene molecules selectively adsorbed on the 1H $PtSe_2$ domains of a 1H/1T patterned $PtSe_2$ film, forming well-ordered triangular clusters. $V_s = -1.6$ V, $I_t = 0.5$ nA. **i**, High-resolution STM image of pentacene molecules selectively adsorbed on one 1H $PtSe_2$ domain. A schematic of a pentacene molecule is shown on the right. $V_s = -1.0$ V, $I = 0.8$ nA.

triangular nanopores is shown in Fig. 3a. The nanopores form a hexagonal lattice as indicated by the green hexagonal lattice matrix with a periodicity of ~3 nm. The figure clearly shows domains with triangular nanopores of opposite orientations, separated by domain boundaries comprising parallelogram-shaped nanopores. High-resolution STM images of a domain-boundary region and a single nanopore are shown in Figs 3b and 3c, respectively. The shape of the nanopores, the honeycomb lattice of CuSe, and the zigzag edges of the nanopore are clearly resolved.

An atomic-resolution STM image of a patterned monolayer CuSe with nanopores is shown in Fig. 3d. Based on a low-energy electron diffraction (LEED) pattern (as shown in Supplementary Fig. 9), a $(4\sqrt{3} \times 4\sqrt{3})$ CuSe sitting on a (11×11) Cu(111) model is proposed. The optimized atomic configuration is shown in Fig. 3f. For better visualization, the Cu(111) substrate is hidden. The simulated STM image based on the proposed atomic model is shown in Fig. 3e, in excellent agreement with the experimental data. Note that the wiggly atomic lines (marked by purple curves in Fig. 3d–f) induced by the release of stress are well reproduced by the DFT simulations.

To further confirm that the fabricated CuSe is a monolayer, we performed a cross-section high-angle annular-dark-field scanning

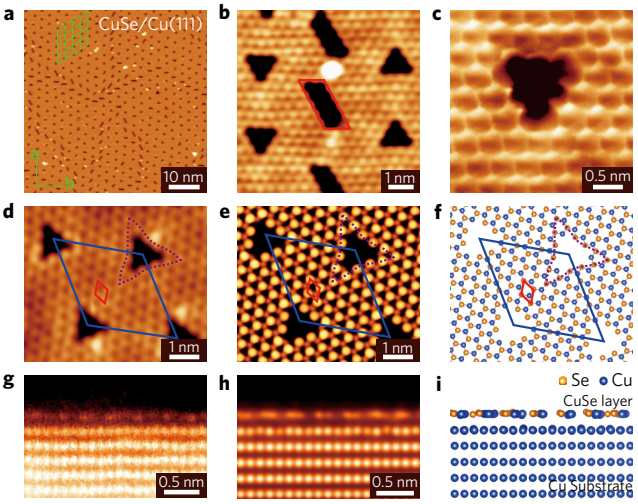

Figure 3 | Patterned CuSe monolayer with periodic nanopores. **a**, A large-scale STM image of patterned CuSe monolayer. The green lattice presents the 3 nm periodicity of the nanopores. $V_s = -1.5$ V, $I_t = 0.1$ nA. **b**, A high-resolution STM image of a domain-boundary region. The boundary consists of parallelogram-shaped nanopores as indicated by the red parallelogram. $V_s = -1.0$ V, $I_t = 0.3$ nA. **c**, A high-resolution STM image of a single nanopore. Honeycomb lattice of CuSe and the zigzag edges of the nanopore are clearly resolved. $V_s = -0.01$ V, $I_t = 7.0$ nA. **d**–**f**, An atomic-resolution STM image (**d**), simulated STM image (**e**), and theoretical model (**f**) of CuSe monolayer on Cu(111) with periodic nanopores. The images show the detailed structure of nanopores. $V_s = -1.0$ V, $I_t = 0.4$ nA. In **f**, Cu substrate is hidden for visualization purposes. **g**–**i**, Cross-section STEM image (**g**), simulated cross-section STEM image (**h**), and side view (**i**) of a CuSe monolayer on a Cu(111) substrate. The STEM image confirms that the patterned CuSe is single layer.

transmission electron microscopy (STEM) study. An experimental image, a simulated image and side view of the structure are shown in Fig. 3g–i, respectively. The excellent agreement further proves that the CuSe pattern with periodic nanopores is a monolayer material.

The periodicity and size of the nanopores can be explained as follows. In principle, the Cu substrate and a CuSe monolayer are incommensurate. The two lattices can be made commensurate, however, if a $(4\sqrt{3} \times 4\sqrt{3})$ CuSe supercell is stretched by 1.5%. This supercell then registers on a (11×11) Cu(111) surface supercell, with a central Cu atom of the monolayer supercell on top of a Cu atom on the substrate. Removal of this central atom and three shells of atoms around it, a total of 13 atoms, produces the observed nanopores at the observed periodicity. In Supplementary Fig. 10, we demonstrate that removal of these 13 atoms amounts to removing three complete hexagonal rings and corresponds to maximum gain of energy (negative formation energy) compared with other options for removing atoms. We conclude that formation of 13-atom nanopores at the observed periodicity is the energetically preferred way to relieve the lattice-mismatch strain.

We have been able to demonstrate selective adsorption on the patterned CuSe monolayer with nanopores. Fe atoms deposited on a CuSe monolayer form W-shape clusters in the nanopore hexagonal superstructure as shown in the large-scale STM image in Fig. 4a. Considering the threefold symmetry of a nanopore, three different orientations of W-shape clusters can be found, as indicated by three 'W' letters in Fig. 4a. DFT calculations suggest that the W-shape cluster contains 13 Fe atoms (the atomic configuration and a discussion about other possibilities are presented in Supplementary Fig. 11). Simulation of the STM image based on this model is provided in Fig. 4c, showing excellent agreement with the atomic-resolution STM image (Fig. 4b). The proposed model is further confirmed by *in situ* XPS measurements. As shown in Fig. 4d, the Fe $2p_{3/2}$ and Fe $2p_{1/2}$ core-level spectra are located at 707.24 eV and 720.40 eV, respectively, which are similar to the Fe $2p$ core levels in bulk FeSe (ref. 22). In addition to the W-shape clusters in the

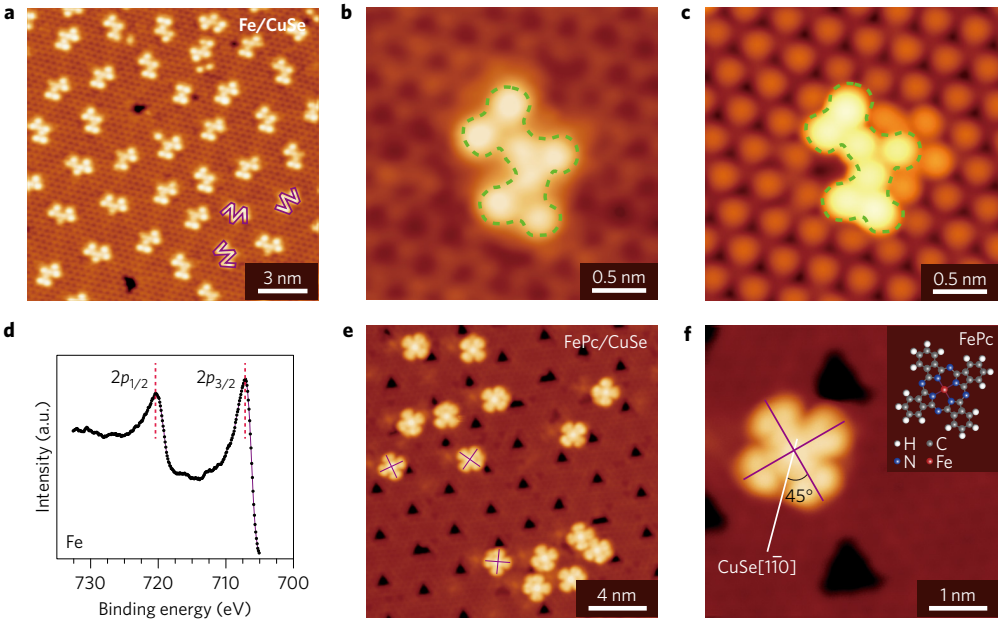

Figure 4 | Selective adsorption on patterned CuSe with periodic nanopores. **a**, A large-scale STM image of CuSe monolayer with W-shaped FeSe clusters. The clusters selectively adsorb in the nanopores of CuSe monolayer. $V_s = -0.1$ V, $I_t = 1.5$ nA. **b**, A high-resolution STM image of the W-shaped cluster. The image shows that the W-shaped cluster contains seven protrusions. $V_s = -0.1$ V, $I_t = 1.5$ nA. **c**, A simulated STM image of an $Fe_{13}Se_7$ cluster in the nanopores. The green contour line and the seven protrusions perfectly match those in **b**. **d**, XPS data showing the Fe $2p_{3/2}$ and Fe $2p_{1/2}$ core levels. **e**, A large-scale STM image of FePc molecules on CuSe. The FePc molecules selectively adsorb on CuSe terraces with preferential orientations as discussed in the text. $V_s = -1.1$ V, $I_t = 0.1$ nA. **f**, High-resolution STM image of a FePc molecule on CuSe. Atomic structure of the FePc molecule is shown in the inset. $V_s = -1.1$ V, $I_t = 1.5$ nA.

periodic nanopores, zigzag-shaped clusters also form in the more extended parallelogram-shaped nanopores at domain boundaries (see Supplementary Fig. 12).

In addition to the selective adsorption in nanopores, additional selective functionalization is achieved by deposition of FePc molecules on the terraces. An atomic model of FePc is shown in the inset of Fig. 4f. As shown in Fig. 4e, when we deposit FePc molecules onto a patterned monolayer CuSe, the molecules are monodispersed and adsorbed only on CuSe terraces. A zoomed-in STM image (Fig. 4f) shows a clear cross feature, which is a typical apparent topography of FePc molecules[23]. It is noticed that FePc molecules on a CuSe substrate have preferred orientations. The angle between FePc molecules (indicated by the sketched purple cross) and the CuSe[1$\bar{1}$0] direction (white line) is ∼45°. As a result of the threefold symmetry of the substrate and the fourfold symmetry of the molecule, there are three equivalent preferred orientations as indicated by the three purple crosses in Fig. 4e.

Comparing the two intrinsically patterned monolayers, that is, 1H/1T $PtSe_2$ and CuSe with periodic nanopores, they are both achieved by direct selenization. After annealing at a high temperature, monolayer 1T $PtSe_2$ undergoes a phase transition and forms the 1H/1T pattern, while periodic nanopores appear in CuSe monolayer. We attribute the difference in the two prototype systems to the interactions between the epitaxial monolayer and the substrate. In the $PtSe_2$/Pt(111) system, the van der Waals interaction between $PtSe_2$ and the Pt substrate gives freedom to flip the structure from 1T to 1H. In contrast, the interaction between CuSe monolayer and a Cu substrate is much stronger. Emission of atoms and formation of nanopores becomes the way to lower the energy.

Both the $PtSe_2$ and CuSe samples are stable in ambient conditions. The samples were removed from the high-vacuum chamber and were kept in air without protection for more than 12 h. The samples were then put back to the high-vacuum chamber and annealed at 200 °C for $PtSe_2$ and 400 °C for CuSe to remove the possible adsorbates. STM images show that the samples keep their patterns (see Supplementary Fig. 13). The stability in air makes these patterned monolayers suitable for potential applications involving ambient conditions.

In summary, we demonstrate a concept of intrinsically patterned 2D materials that can be selectively functionalized. We demonstrate the fabrication of patterned 2D monolayers in two cases: 1H/1T monolayer $PtSe_2$ tiling pattern and monolayer CuSe with periodic nanopores. Selective adsorptions are achieved in both cases. This work ushers in a frontier for the fabrication of intrinsically patterned 2D materials.

Methods

Methods, including statements of data availability and any associated accession codes and references, are available in the online version of this paper.

Received 5 January 2017; accepted 3 May 2017; published online 12 June 2017

References

1. Novoselov, K. S. *et al*. A roadmap for graphene. *Nature* **490,** 192–200 (2012).
2. Oughaddou, H. *et al*. Silicene, a promising new 2D material. *Prog. Surf. Sci.* **90,** 46–83 (2015).
3. Desai, S. B. *et al*. MoS_2 transistors with 1-nanometer gate lengths. *Science* **354,** 99–102 (2016).
4. Chhowalla, M. *et al*. The chemistry of two-dimensional layered transition metal dichalcogenide nanosheets. *Nat. Chem.* **5,** 263–275 (2013).
5. Yin, K. Unsupported single-atom-thick copper oxide monolayers. *2D Mater.* **4,** 011001 (2017).
6. Geim, A. K. & Grigorieva, I. V. Van der Waals heterostructures. *Nature* **499,** 419–425 (2013).
7. Eda, G. *et al*. Coherent atomic and electronic heterostructures of single-layer MoS_2. *ACS Nano* **6,** 7311–7317 (2012).
8. Withers, F. Light-emitting diodes by band-structure engineering in van der Waals heterostructures. *Nat. Mater.* **14,** 301–306 (2015).
9. Jung, M. W. *et al*. Novel fabrication of flexible graphene-based chemical sensors with heaters using soft lithographic patterning method. *ACS Appl. Mater. Interfaces* **6,** 13319–13323 (2014).
10. Joshi, S. *et al*. Control of molecular organization and energy level alignment by an electronically nanopatterned boron nitride template. *ACS Nano* **8,** 430–442 (2014).
11. Cho, S. *et al*. Phase patterning for ohmic homojunction contact in $MoTe_2$. *Science* **349,** 625–628 (2015).
12. Voiry, D. *et al*. The role of electronic coupling between substrate and 2D MoS_2 nanosheets in electrocatalytic production of hydrogen. *Nat. Mater.* **15,** 1003–1009 (2016).
13. Pan, L. D., Zhang, L. Z., Song, B. Q., Du, S. X. & Gao, H.-J. Graphyne- and graphdiyne-based nanoribbons: density functional theory calculations of electronic structures. *Appl. Phys. Lett.* **98,** 173102 (2011).
14. Gao, G., Jiao, Y., Waclawik, E. R. & Du, A. Single atom (Pd/Pt) supported on graphitic carbon nitride as an efficient photocatalyst for visible-light reduction of carbon dioxide. *J. Am. Chem. Soc.* **138,** 6292–6297 (2016).
15. Zhang, H., Li, Y., Hou, J., Tu, K. & Chen, Z. FeB_6 monolayers: the graphene-like material with hypercoordinate transition metal. *J. Am. Chem. Soc.* **138,** 5644–5651 (2016).
16. Pan, Y. *et al*. Highly ordered, millimeter-scale, continuous, single-crystalline graphene monolayers formed on Ru(0001). *Adv. Mater.* **21,** 2777–2780 (2009).
17. Lee, M. *et al*. Ballistic miniband conduction in a graphene superlattice. *Science* **353,** 1526–1529 (2016).
18. Huang, S. *et al*. Ultrathin $FeSe_2$ nanosheets: controlled synthesis and application as a heterogeneous catalyst in dye-sensitized solar cells. *Chem. Eur. J.* **21,** 4085–4091 (2015).
19. Wang, Y. *et al*. Monolayer $PtSe_2$, a new semiconducting transition-metal-dichalcogenide, epitaxially grown by direct selenization of Pt. *Nano Lett.* **15,** 4013–4018 (2015).
20. Lin, J., Pantelides, S. T. & Zhou, W. Vacancy-induced formation and growth of inversion domains in transition-metal dichalcogenide monolayer. *ACS Nano* **9,** 5189–5197 (2015).
21. Lin, Y. C., Dumcenco, D. O., Huang, Y. S. & Suenaga, K. Atomic mechanism of the semiconducting-to-metallic phase transition in single-layered MoS_2. *Nat. Nanotech.* **9,** 391–396 (2014).
22. Yamasaki, A. Electron correlation in the FeSe superconductor studied by bulk-sensitive photoemission spectroscopy. *Phys. Rev. B* **82,** 184511 (2010).
23. Cheng, Z. H. *et al*. High resolution scanning-tunneling-microscopy imaging of individual molecular orbitals by eliminating the effect of surface charge. *Surf. Sci.* **605,** 415–418 (2011).

Acknowledgements

We acknowledge the financial support from National Key Research and Development Projects of China (2016YFA0202300), the National Basic Research Program of China (2013CBA01600), the National Natural Science Foundation of China (Nos 61390501, 51572290, 61306015 and 61471337, 51325204) and the Chinese Academy of Sciences (Nos 1731300500015, XDB07030100, and the CAS Pioneer Hundred Talents Program). A portion of the research was performed in CAS Key Laboratory of Vacuum Physics. Work at Vanderbilt (S.T.P. and Y.Y.Z.) was supported by the US Department of Energy under grant DE-FG02-09ER46554 and by the McMinn Endowment. Computations by Y.Y.Z. were carried out at the National Energy Research Scientific Computing Center, a DOE Office of Science User Facility supported by the Office of Science of the US Department of Energy under Contract No. DE-AC02-05CH11231. The electron microscopy work was supported in part by the US Department of Energy, Office of Science, Basic Energy Science, Materials Sciences and Engineering Division, and through a user project at ORNL's Center for Nanophase Materials Sciences, which is a DOE Office of Science User Facility.

Author contributions

H.-J.G. and S.T.P. conceived and coordinated the research project. X.L. designed the CuSe experiments. J.C.L. and K.Q. prepared CuSe samples and performed the STM experiments. Y.L.W. designed the $PtSe_2$ experiments. Y.S., X.W., S.Y.Z., L.F.L., Y.Q.W., Z.L.L. and H.M.G. prepared $PtSe_2$ samples and performed the STM experiments. T.L., C.L., J.O.W. and K.I. provided support for XPS experiments. D.N.L. and W.Z. performed the STEM experiments. Y.Y.Z., J.B.P., L.G., Y.F.Z., D.L.B. and J.T.S. performed the DFT calculations under the guidance of S.X.D. All authors participated in discussing the data and editing the manuscript.

Additional information

Supplementary information is available in the online version of the paper. Reprints and permissions information is available online at www.nature.com/reprints. Publisher's note: Springer Nature remains neutral with regard to jurisdictional claims in published maps and institutional affiliations. Correspondence and requests for materials should be addressed to Y.L.W., S.X.D. or H.-J.G.

Competing financial interests

The authors declare no competing financial interests.

Methods

Preparation of 1H/1T $PtSe_2$ on Pt(111) substrate by transforming from 1T $PtSe_2$. Single-layer 1T $PtSe_2$ films were grown in a commercial ultrahigh-vacuum (UHV) system (Omicron), with a base pressure better than 3×10^{-10} mbar, equipped with standard molecular beam epitaxy capabilities. The Pt(111) substrate was cleaned by several cycles of argon-ion sputtering followed by annealing until sharp (1×1) diffraction spots in the LEED pattern and clean surface terraces in the STM images were obtained. High-purity Se (99.99%, Sigma-Aldrich) evaporated from a Knudsen cell was deposited onto the clean Pt(111) surface at room temperature. The sample was subsequently annealed up to 270 °C to achieve selenization and crystallization, which leads to homogeneous 1T $PtSe_2$ films on Pt(111) substrate. By annealing this sample at 400 °C, the 1T $PtSe_2$ transforms to the 1H/1T $PtSe_2$ with triangular patterns.

Preparation of 1H/1T $PtSe_2$ on Pt(111) substrate by controlling the Se initial density. As shown in Supplementary Fig. 4, an alternative method to produce the 1H/1T triangular pattern is to control the Se initial density. Having obtained the clean Pt(111) surface, the crucible filled with the Se source was aligned at the edge instead of the centre of the substrate during the fabrication process. This off-centre alignment leads to varying initial density of Se atoms at different regions of the substrate, resulting in a Se density gradient. The sample was subsequently annealed up to 270 °C to achieve selenization and crystallization, which finally leads to different structures. A triangular tiling pattern of 1H/1T $PtSe_2$ forms in the area with a relatively low initial Se density. As the density of Se atoms increases, the size of 1T $PtSe_2$ triangles increases and the number of 1H $PtSe_2$ triangles decreases significantly. As the Se density increases further, it finally leads to a defect-free homogeneous 1T $PtSe_2$ film.

Preparation of patterned CuSe, Fe/CuSe and FePc/CuSe on Cu(111) substrate. The growth of 2D patterned CuSe was carried out in a commercial UHV system (Omicron) (base pressure better than 1×10^{-10} mbar) equipped with a sample preparation chamber. Clean single-crystal Cu(111) (MaTecK) surface was obtained via cycles of argon-ion sputtering followed by annealing at 550 °C. The cleanliness of the Cu(111) surface was verified by STM scanning. The 2D patterned CuSe sample was obtained by Se (99.99%, Sigma-Aldrich) deposition from a standard Knudsen cell while the Cu substrate was held at room temperature, and post-annealing at 200 °C. For the Fe/CuSe and FePc/CuSe samples, the beam of Fe (99.99%, ESPI) and the FePc molecules (99.99%, Sigma-Aldrich) were generated from a commercially available electron-beam cell (Omicron) and a standard Knudsen cell, respectively. During the deposition, the patterned CuSe sample was kept at room temperature. After preparation, the samples were transferred to the low-temperature STM head operating at ~4 K.

***Ex situ* STEM characterization of CuSe on Cu(111) substrate.** *Cross-section TEM sample preparation.* A layer of amorphous carbon of ~100 nm in thickness was first deposited onto the as-grown CuSe monolayer on a Cu substrate shortly after removal from the MBE chamber. A TEM cross-section sample was prepared along the Cu[112] zone axis using a focused ion beam and was further thinned to ~40 nm thick using low-energy ion milling. *STEM-ADF* (*scanning transmission electron microscopy-annular dark field*) *imaging.* The experimental STEM-ADF imaging was performed on an aberration-corrected Nion UltraSTEM-100 operated at 100 kV. The convergence semi-angle was set to 30 mrad, and the ADF images were collected from ~80–200 mrad semi-angle range. The thickness of the cross-section sample was measured to be ~40 nm using electron energy-loss spectroscopy. STEM-ADF image simulation was performed using QSTEM with the same accelerating voltage, probe-forming angle and detector angle as those used in experiment. A single-crystal CuSe domain was used in the simulation, with the thickness of the cross-section sample set to 22 nm.

STM and LEED measurements of the as-grown samples. STM images of the samples were acquired in the constant-current mode, using an electrochemically etched tungsten tip. All voltages were applied to the sample with respect to the tip. The Nanotec Electronica WSxM software was used to process the STM images. Low-energy electron diffraction (LEED) was employed with a 4-grid detector (Omicron Spectra LEED) in a connected UHV chamber to identify the superstructure macroscopically.

XPS measurements of the as-grown samples. The *in situ* X-ray photoelectron spectroscopy (XPS) measurements of the samples were conducted at the Beijing Synchrotron Radiation Facility (BSRF). After growth, the samples were transferred by a UHV suitcase to the XPS station for measuring the change of chemical states of elements. The monochromatic synchrotron radiation is realized by four high-resolution gratings and is controlled by a hemispherical energy analyser. The photon energy is in the range from 10 to 1,100 eV.

Theoretical calculations. Quantum mechanical calculations based on density functional theory (DFT) are performed using the Vienna *ab initio* simulation package (VASP)[24,25]. The projector augmented wave method is employed to describe the core electrons. The local density approximation (LDA)[26,27] is used for exchange and correlation. The rotationally invariant LDA+U formalism proposed in ref. 28 is used and U_{eff} is chosen as 6.52 eV and 4.3 eV for Cu and Fe respectively[29]. The electronic wavefunctions are expanded in plane waves with a kinetic energy cutoff of 400 eV. The periodic slab models of $PtSe_2$/Pt(111) include four layers of (4×4) Pt(111) substrate, and a monolayer of (3×3) $PtSe_2$. The k-points sampling is $5 \times 5 \times 1$, generated automatically with the origin at the Γ-point. The periodic slab models of CuSe/Cu(111) include three layers of (11×11) Cu(111) and $(4\sqrt{3} \times 4\sqrt{3})$ CuSe. The k-points sampling is $1 \times 1 \times 1$. For all of the calculations, the bottom two layers of substrate atoms are fixed, while all the other atoms are fully relaxed. The structures were relaxed until the energy and residual force on each atom were smaller than 10^{-4} eV and 0.02 eV $Å^{-1}$, respectively. The vacuum layers of the two models are larger than 15 Å. The STM simulations are performed using the Tersoff–Hamann approach[30].

Data availability. The data that support the findings of this study are available from the corresponding author on reasonable request.

References

24. Kresse, G. & Furthmüller, J. Efficiency of *ab-initio* total energy calculations for metals and semiconductors using a plane-wave basis set. *Comput. Mater. Sci.* **6,** 15–50 (1996).
25. Kresse, G. & Furthmüller, J. Efficient iterative schemes for *ab initio* total-energy calculations using a plane-wave basis set. *Phys. Rev. B* **54,** 11169–11186 (1996).
26. Ceperley, D. M. & Alder, B. J. Ground state of the electron gas by a stochastic method. *Phys. Rev. Lett.* **45,** 566–569 (1980).
27. Perdew, J. P. & Zunger, A. Self-interaction correction to density-functional approximations for many-electron systems. *Phys. Rev. B* **23,** 5048–5079 (1981).
28. Dudarev, S. L., Botton, G. A., Savrasov, S. Y., Humphreys, C. J. & Sutton, A. P. Electron-energy-loss spectra and the structural stability of nickel oxide: an LSDA+U study. *Phys. Rev. B* **57,** 1505–1509 (1998).
29. Cococcioni, M. & de Gironcoli, S. Linear response approach to the calculation of the effective interaction parameters in the LDA+U method. *Phys. Rev. B* **71,** 035105 (2005).
30. Tersoff, J. & Hamann, D. R. Theory of the scanning tunneling microscope. *Phys. Rev. B* **31,** 805–813 (1985).